# Phase-locking behaviors in an ionic model of sinoatrial node cell and tissue

Xiaodong Huang,[1] Yuanyuan Mi,[1] Yu Qian,[2] and Gang Hu[1,3,*]

[1]*Department of Physics, Beijing Normal University, Beijing 100875, China*

[2]*Nonlinear Research Institute, Baoji University of Arts and Sciences, Baoji 721007, China*

[3]*Beijing-Hong Kong-Singapore Joint Center of Nonlinear and Complex Systems, Beijing Normal University Branch, Beijing, China*

(Received 6 July 2010; revised manuscript received 4 May 2011; published 27 June 2011)

Phase-locking behaviors in sinoatrial node (SAN) are closely related to cardiac arrhythmias. An ionic model considering structural heterogeneity of SAN is numerically investigated. The bifurcations between phase-locking zones are interpreted by the map derived from the phase resetting curve. Furthermore, the validity of the circle map in describing phase locking of the actual SAN system is evaluated and explained. We reveal also how the phase-locking behaviors in heterogeneous tissue depend on the location of stimulating site and the coupling strength of the tissue. All these results may be of suggestive uses for understanding and controlling practical SAN dynamics.

DOI: 10.1103/PhysRevE.83.061917 PACS number(s): 87.19.Hh, 05.45.−a

## I. INTRODUCTION

The sinoatrial node (SAN), which produces rhythmic beats, is the normal pacemaker of the heart. The behaviors of SAN are closely related to the arrhythmias resulting from abnormal impulse initiations [1]. The beating rate of SAN is regulated by multiple factors [2], such as noradrenaline released by sympathetic nerve, acetylcholine released by vagal nerve, and even some feedback from the atria and ventricles (e.g., spiral waves in atrium may be a possible source of external stimulation). Therefore, the heart rate is the result of the interactions between SAN cell dynamics and the stimulations [3–5]. Investigation of the behaviors of periodically stimulated SAN tissue is thus of great significance for understanding arrhythmias and their treatments.

Mobitz [6] and van der Pol and van der Mark [7] were the first to employ nonlinear models to investigate cardiac behaviors. The development of nonlinear dynamics greatly promoted the research of biological systems [8–12]. The responses of the oscillators to stimulations are assumed to be closely related to biological rhythm. Studying the dynamic characteristics of periodically stimulated SAN model is the object of the present paper.

Phase-locking behavior is an important nonlinear dynamic feature in biological oscillators. It indicates the entrainment between the system and the external stimulations, and determines the rhythm of the system [13–15]. In the theoretical researches of phase-locking behaviors, a circle map has been popularly used as a standard model [13,16], which predicts various bifurcations leading to rich phase-locking states. Many of these predictions are in accordance with the phenomena observed in experiments [13,14]. The phase-resetting relation, which depicts the interaction between the oscillation and external stimulations, is an intrinsic property of biological oscillators [17]. It is well known that a brief current pulse applied to an oscillatory cell or model can shift the phase of the oscillation in varieties of biological systems [15,18–22]. The magnitude and direction of the phase shift (i.e., phase resetting) depend on the phase and amplitude of the stimulus applied. The relation between the phase of the stimulus and the resulted phase shift is called the phase-resetting relation. The phase-resetting relation has been used to interpret the entrainment properties of SAN cells [14,23,24]. Based on the relation, a circle map can be derived (some authors called it phase resetting map [25] (PRM), which will be introduced in the section of method). PRM is a well-defined technique for investigating biological dynamics. The graphic approach of PRM to investigate phase lockings was developed from the research of simple oscillator models [26–28] and experimental cardiac cell aggregates [15,18,29,30]. They revealed that bifurcations and related phase lockings are determined by the topology of PRM. In SAN systems, the PRM approach has been used to investigate the entrainment of a stimulated single SAN cell and ionic model [14,22].

The sinoatrial node is a typical oscillatory medium and much effort has been done in understanding its behaviors and the related arrhythmias (see review [2]). In the previous studies, theoretical investigations describing the phase lockings of SAN were carried out with some simplified and ideal models, where actual physiological parameters were seldom considered. On the other hand, experiments were done in single cells or isolated pieces of tissue [14,31]. However, SAN tissue consists of coupled cells which have different dynamical properties and thus the tissue has a heterogeneous structure [32]. The phase-locking structure of the heterogenous SAN tissue has not yet been systematically investigated. The PRM technique is applied to analyze phase lockings of the present SAN model. We intend to shed light on the above problems in the present work.

We numerically investigate phase-locking behaviors in an ionic SAN model which considers the heterogeneity of SAN [33]. The major results of our work are: (i) The phase-locking structures of central and peripheral SAN cells are elucidated. (ii) The graphic approach by PRM to describe the phase-locking behaviors is discussed. Phase-resetting maps are classified by the shape, which has been referred to topological degree by Winfree and some other authors [17,28], to identify phase-locking properties. (iii) The validity and failure of the map description are evaluated. (iv) The characteristics and the relevant factors of the phase-locking

*ganghu@bnu.edu.cn

 

behaviors in heterogeneous tissue are revealed, which indicate that the phase-locking behaviors depend on the locations of stimulating site and the coupling strength as well as the amplitude. As the model is regarded to be close to the practical SAN situation, investigation of such a system in a large scale of parameters may provide some instructive suggestions for practical operations.

## II. MODEL AND METHODS

In the present paper, we investigate phase-locking behaviors of single cell and one-dimensional (1D) cable of a heterogeneous SAN model developed by Zhang *et al.* [33], and interpret the results by a simplified 1D map derived from the phase-resetting property (called phase-resetting map—PRM) of the model. In this section, the model and derivation of PRM will be introduced. All the equations of the model used in our work are listed in the Appendix. The parameters used in the present model are identical to that given by Ref. [33] unless specified otherwise (see Appendix). The basic features of the present model agree well with the previous experimental and theoretical results [14,32,34]. Moreover, the characteristic properties of the SAN system hold when the parameters are changed in an appropriate range. Therefore, the numerical results are robust.

### A. The gradient model of SAN

Hitherto there are two popular viewpoints of the makeup of SAN: the mosaic model [35] and the gradient model [33]. The mosaic model considers that the SAN tissue is a mixture of automatic pacemaker cells and nonoscillatory atrial cells, where the ratio of pacemaker cells is high in the center and low in the periphery. On the other hand, in the gradient model, the electrical property of SAN cell changes gradually from center to periphery. Zhang *et al.* [36] compared the two models and found that the gradient model coincides better with experiment results. In the present study, we perform the numerical simulations by using a gradient model proposed in Ref. [33] to study the phase-locking problem of SAN cell and tissue.

The differential equation for the dynamics of the cell's membrane potential $V$ (mV) reads

$$C_m \frac{dV}{dt} = -I_{\text{ion}} + I_{st}(t), \tag{1}$$

where $C_m$ is the membrane capacitance, which is 20 pF for single central cell and 65 pF for single peripheral cell, $I_{\text{ion}}$ (nA) is the total transmembrane ionic current, and $I_{st}$ (nA) is the stimulating current. The total ionic current $I_{\text{ion}}$ is the summation of 13 individual ionic currents [33]:

$$\begin{aligned} I_{\text{ion}} = {} & I_{\text{Na}} + I_{\text{Ca,L}} + I_{\text{Ca,T}} + I_{\text{to}} + I_{\text{sus}} + I_{\text{K,r}} + I_{\text{K,s}} + I_{\text{f}} \\ & + I_{\text{b,Na}} + I_{\text{b,Ca}} + I_{\text{b,K}} + I_{\text{NaCa}} + I_{\text{p}}. \end{aligned} \tag{2}$$

Each ionic current in Eq. (2) is usually expressed as

$$I_z = f_z(\mathbf{y}, V) g_z (V - E_z). \tag{3}$$

$I_z$ represents any kind of ionic current, $g_z$ is the membrane conductance of ion $z$, $E_z$ is the equilibrium potential, and $f_z(\mathbf{y}, V)$ is a function of $V$ and the gating variables $\mathbf{y}$ with $\mathbf{y} = (m, h_1, h_2, f_L, d_L, f_T, d_T, q, r, p_{a,f}, p_{a,s}, p_i, x_s, y)$. Each gating variable evolves according to

$$\frac{dy}{dt} = \frac{y_\infty - y}{\tau_y}, \tag{4}$$

where $y$ represents any gating variable, $\tau_y$ and $y_\infty$ are the time constant and the steady state of $y$, respectively. Specifically, we replace some equations about $\tau_y$ and $y_\infty$ of Ref. [33] by equations taken from another model [37], which is an extension of Zhang's SAN model. The integral list of all the equations about $I_z$, $\tau_y$, and $y_\infty$ used in the present work are given in the Appendix. The differences of capacitance and ionic conductance (see the Appendix for their values) between the central and peripheral cells yield the heterogeneity of SAN tissue.

The gradient 1D tissue model is represented by a partial differential equation (PDE):

$$C_m(x) \frac{\partial V(x,t)}{\partial t} = -I_{\text{ion}} + I_{\text{couple}} + I_{st}(x,t). \tag{5}$$

In Fig. 1 the spatial structure of the SAN cable model is illustrated. As indicated by Ref. [33], from a central cell (the top cell labeled "c" in Fig. 1) to peripheral cell (the bottom cell labeled "p" in Fig. 1), the capacitance changes from 20 pF to 65 pF, and the ionic conductance of the membrane varies.

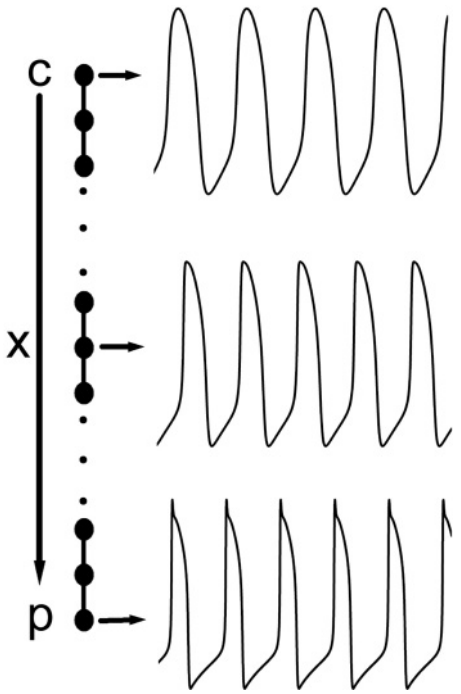


FIG. 1. Illustration of the heterogeneous SAN tissue. The black disks on the left represent SAN cells in the tissue. From top to bottom, the cells vary gradually from central cell to peripheral cell. The coupling strength between neighboring cells (connected by solid line) is $G_{\text{cpl}}$. In the case that $G_{\text{cpl}} = 0$, the action potentials of the cells at central end, middle, and peripheral end of the cable is shown on the right side. The action potentials of different cells are plotted in the same time interval.

The capacitance of the cell at distance $x$ from the central end is thus set by

$$C_m(x) = 20 + \frac{1.07(x-0.1)}{L[1+0.7745e^{-(x-2.05)/0.295}]}(65-20), \quad (6)$$

and the conductance of each current reads

$$g_z(x) = \frac{[65-C_m(x)]g_{zc} + [C_m(x)-20]g_{zp}}{65-20}, \quad (7)$$

where $L$ is the total length of the tissue, $g_{zc}$ and $g_{zp}$ represent conductances of the central end and peripheral end cell, respectively. In Fig. 1 the action potentials of cells at different sites in the tissue are shown, which are determined by the gradient electrophysiology properties.

Equations (1) and (5) are integrated by the explicit Euler method with time step $\Delta t = 0.02$ ms. The gating variable equation is solved by the method developed by Moore and Ramon [38] and Rush and Larsen [39]. In simulations of SAN tissue, space step $\Delta x = 0.1$ mm is used, and the tissue length is $L = 3$ mm (30 grid points). The discretization of time $\Delta t$ and space $\Delta x$ are chosen on the same order of magnitude as those previously used in Ref. [40]. A no-flux boundary condition is used. Stimulation $I_{st}(x,t)$ takes the form of pulsatile stimuli with 2 ms duration and is applied at either end. Each grid point in the cable evolves according to Eq. (5) and its capacitance and conductance parameters are determined by Eqs. (6) and (7). The coupling current is $I_{\text{couple}} = G_{\text{cpl}}[V(i+1) + V(i-1) - 2V(i)]$, where $i$ represents the $i$ th grid point in the cable and $G_{\text{cpl}}$ (nS) is the coupling conductance between neighboring grid points. $G_{\text{cpl}}$ is adjustable and set to be uniform along the cable. The initial values for simulation are given in the Appendix. For each step of simulation in both single cell and cable, initial values are reset to these values. In every time of simulation, transient states are discarded and the data are recorded then.

The entrainment is evaluated by the following way: During one time of oscillation of potential $V$, an action potential is defined if the two conditions, the lowest value (the maximum diastolic potential) is smaller than $-40$ mV and the highest value (the overshoot potential) is larger than $-10$ mV, are both satisfied. Otherwise the oscillation will be regarded as supra- or infrathreshold responses (1:0 is an example of such a state). We use the peak to position an action potential. The time interval between the ($i$-1)th and $i$th peaks of action potential is defined as $T_i$, and the stimulating period is $T_{sti}$. If the equation

$$NT_{sti} = \sum_{i=1}^{M} T_i \quad (8)$$

holds and $N$ and $M$ are integers, then ab $N:M$ state is realized (i.e., there are $N$ input periods and $M$ AP overshoots in a single output phase-locking period). Otherwise, it is a quasiperiodic or chaotic state. Such a way of evaluation is essentially the way to calculate rotation number [26,28], which will be introduced in Sec. II B.

### B. Phase-resetting curve and phase-resetting map

A brief stimulus with a certain amplitude delivered to an oscillatory cell may trigger phase shift of the oscillation, and this phenomenon is called phase resetting [17]. Figure 2 is a brief introduction of such a property. The stimulus applied at phase $\phi$ shifts the phase of the oscillation by $\Delta\phi$ (the solid trace represents the shifted oscillation and the dashed one represents the free-running case), where $\phi$ and $\Delta\phi$ are expressed by the following way: If the time interval between the stimulus and the previous overshoot potential is defined to be $T_s$, and the time interval between the shifted and the original overshoots is defined to be $\Delta T_0$, then the ratio of $T_s$ to the cycle length $T_0$ is $\phi$ ($\phi = T_s/T_0$) and the ratio of $\Delta T_0$ to $T_0$ is $\Delta\phi$ [$\Delta\phi = \Delta T_0/T_0$ (mod 1)]. So that the absolute value of any $\phi$ and $\Delta\phi$ is between 0 and 1. If we scan $\phi$ in the entire cycle and plot $\Delta\phi$ as a function of $\phi$, the phase resetting curve (PRC) is derived. Moreover, the stimulus amplitude can also change $\Delta\phi$ and PRC is thus a function of amplitude [22].

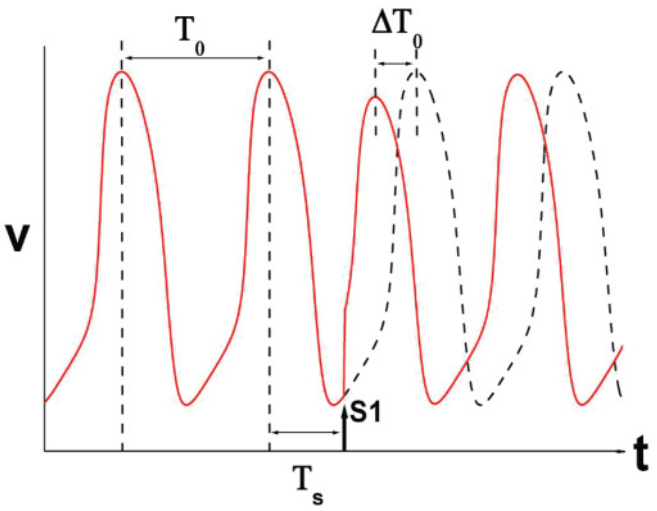


FIG. 2. (Color online) Phase resetting property of a SAN cell. The dashed trace represents the free-running oscillation. The solid trace represents the phase response to the application of S1. $T_s$ is the time applying a stimulus and $\Delta T_0$ is the time shift responding to the stimulus. $\phi = T_s/T_0$ is the phase of the stimulus, and $\Delta\phi = \Delta T_0/T_0$ (mod 1), which is a function of $\phi$ and the amplitude of stimulus, is the phase shift triggered by S1.

Based on the PRC, the so-called PRM is derived [18,26–28], and PRM is significant for analyzing entrainment. To be instructive, we introduce the deduction of PRM briefly. From Fig. 2 we know that if another stimulus (S2) is delivered at time interval $T_{sti}$ relative to S1 stimulus, the phase of S2 relative to the shifted oscillation (the solid configuration) is represented by $\phi_{S2} = \phi - \Delta\phi + T_{sti}/T_0$ (mod 1). The operation mod 1 is due to that the phase is expressed as the ratio of $T_0$, which is the time interval between successive action potential overshoots. It is defined that $g(\phi) = \phi - \Delta\phi$ (mod 1). A map based on the phase resetting effect is finally derived as

$$\phi_{i+1} = g(\phi_i) + \frac{T_{sti}}{T_0}(\text{mod}1), \quad (9)$$

which is a circle map. Equation (9) is called the phase-resetting map (PRM). It should be noted that $\Delta\phi$ may be different if it is measured by different action potentials after stimulation [17,21]. In our work, we use the first action potential (shown

by Fig. 1) to determine $\Delta\phi$. Based on Eq. (9), the rotation number is defined as $\rho = \frac{M}{N}$, where $M$ and $N$ satisfy

$$M = \sum_{i=1}^{N} g(\phi_i) + \frac{T_{sti}}{T_0} - \phi_i. \tag{10}$$

If $M$ is an integer, rational $N : M$ phase locking holds. Other wise, it is a quasiperiodic or chaotic state.

## III. PHASE-LOCKING STRUCTURES OF THE SINGLE CENTRAL AND PERIPHERAL CELLS

In the studies of circle map, Arnol'd tongue (AT) is the typical structure representing phase locking behaviors [41]. The AT structure reveals that: As the driving amplitude is increased, the phase-locking zones are enlarged, which look like tongues growing from the bottom to the top in the "$\omega$-A" plane ($\omega$ on the abscissa represents the driving frequency and A on the ordinate represents the driving amplitude). A number of previous works analyzed the ATs of different oscillators, and revealed the routes to phase locking, quasiperiodic, and chaotic motions for various biological systems [8,13,16,25–28,42,43]. In this section, we perform direct simulations in the ionic SAN model [Eq. (1)] and elucidate the ATs of such a single-cell system.

It was experimentally found that the intrinsic oscillatory frequencies of the central SAN cells are slower than those of the peripheral ones, and the action potential configurations of the two types of cells are different [32]. The intrinsic oscillation periods of central and peripheral cells (the top and bottom cell in Fig. 1, respectively) of the present model are 299 ms and 236 ms, respectively. The action potential traces of the central and peripheral cells are shown in Fig. 3(a). Figure 3(b) shows the projections of the stable limit cycles of the two instances in a phase plane constructed by membrane potential $V$ and the total ionic current $I_{\text{ion}}$, which has been used by Clay *et al.* [44] to analyze considerable amount of phase resetting properties of self-oscillatory heart cell aggregates. We numerically find that there is a stable focus (−33.1,0) for central cell [Fig. 3(c)] as well as an unstable focus (−39.8,0) for peripheral cell [Fig. 3(d)] in the phase plane. The stability is verified by numerical computations of the eigenvalues of the Jacobian matrix of the fixed points (see the Appendix). In a central cell, there may be an unstable limit cycle separating the stable focus and stable limit cycle. The unstable limit cycle may yield a transition from a degree 1 PRM to a PRM of undetermined type to a degree 0 PRM [45]. The central stable focus has a narrow basin of attraction in phase space, so that properly chosen initial values, or stimulus with proper amplitude delivered at proper phases may bring the trajectory into the basin of attraction, and annihilation occurs [34]. But the oscillation of peripheral cell cannot be annihilated due to the unstable focus. It should be noted that the basin structures may be very complex in high-dimensional phase space for the central cell. If the number of equilibrium point in phase space is larger than one, more complex phenomena will occur [46].

Figures 4(a) and 4(b) show the ATs of the central and peripheral cells, respectively. The characteristics of the phase-locking behaviors can be summarized as: (i) At low amplitude of stimulation, the $N : M$ ATs normally grow, and the order

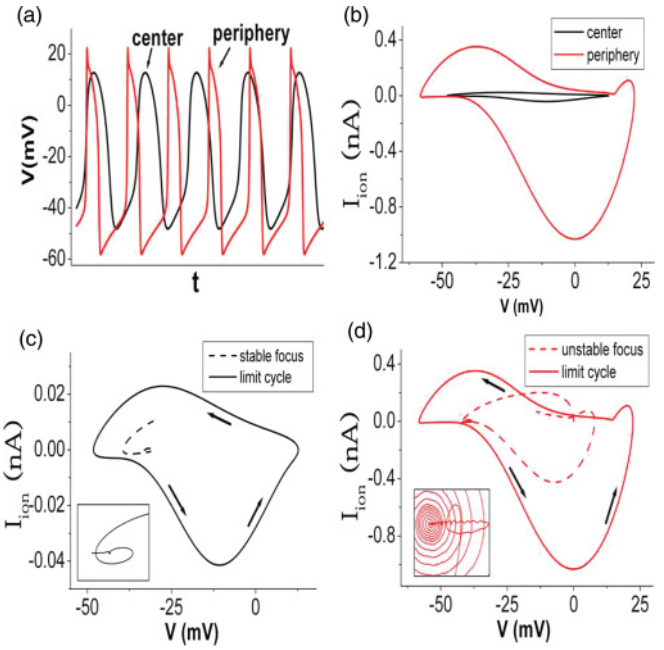


FIG. 3. (Color online) Automatic action potentials of central and peripheral cells and attractors in phase plane. (a) Action potential configurations. The central cell beats at a lower frequency, and its AP has a lower overshoot, maximum diastolic potential, and diastolic depolarization rate. The upstroke similar with that observed in atrial cells is observed in peripheral SAN cell, which indicates that the peripheral cells possess properties of the neighboring atrial cells. (b) Projections of the limit cycles of both cells in phase plane. The smaller cycle represents the central case while the larger cycle represents the peripheral case. (c), (d) The nature of the attractors: a stable limit cycle with a stable focus for central cell and a stable limit cycle with an unstable focus for peripheral cell. The insets of (c) and (d) are the enlargements of the fixed point vicinity. The arrows point out the direction of movement of the state point along the limit cycle.

of the phase locking ratio follows the Farey's tree sequence [i.e., there is an $(N_1 + N_2):(M_1 + M_2)$ AT between $N_1 : M_1$ and $N_2 : M_2$ ATs]. (ii) As amplitude is increased, only the $N : 1$ (and $2N : 2$, which occur from $N : 1$ via period doubling bifurcation) ATs can develop and all other complex $N : M$ ($M > 1$) ATs become very narrow, and finally only some simple phase-locking zones (e.g., 1:1, 2:2, and 2:1) remain for sufficiently large amplitude. Specifically, if the cell oscillates at a period identical to the stimulating period, and the stimulating period is far below the real 1:1 region (a real 1:1 region should locate around the intrinsic period of the cell), the phase locking is determined as a 1:0 state. In this situation of very fast stimulating, the cell oscillates periodically on a stable cycle, which should be regarded as supra- or infrathreshold responses rather than action potentials. Moreover, the 1:0 state can also be predicted by PRM [Eq. (9)], which requires $\Delta\phi = T_{sti}/T_0$.

The previous studies clearly revealed the very fine structures of the ATs in diverse systems [13,26,27,30]. The also found the multistability of the phase-locking states [28,42]. In the present paper, we do not intend to depict such fine structures of phase locking. Since that we reset the initial values for each step of simulation as stated in Sec. II, multistability is not

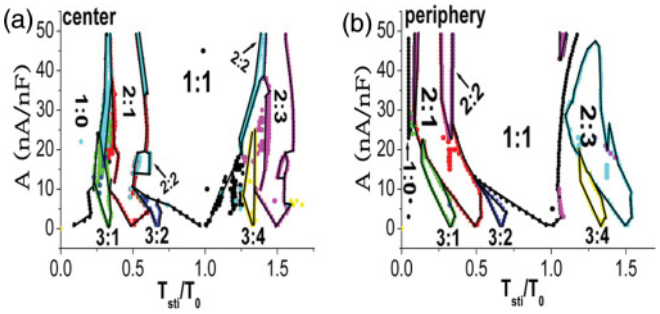


FIG. 4. (Color online) Phase-locking structures of single-central and peripheral cells, which are illustrated by (a) and (b), respectively. Capacitance is 20 pF for center cell and 65 pF for periphery cell. Intrinsic period of the cells are 299 ms for center and 236 ms for periphery. The abscissa is the ratio of the stimulating period to the intrinsic period of the cell. The zones plotted are part of the overall phase locking zones. The colors are for distinguishing the zones from each other. At low amplitude, ATs following Farey's tree can be seen. At high amplitude, complex $N : M$ ($M > 1$) ATs become very narrow and simple $K + N : 1$ (and $K + 2N : 2, K = 0,1\ldots$) ATs remain eventually.

shown and discussed. The aim of Fig. 4 is to show the tendency of the ATs and the comparison of phase locking behaviors between central and peripheral cells. The consistency between the previous works and the present work lends support to the contention that the nature of the response is generic in varieties of biological systems.

Intuitively speaking, the $N : 1$ phase lockings at high-stimulation amplitude are significant for the function of SAN. Simple $N : 1$ lockings can maintain regular beat-to-beat interval and thus the heart rhythm is still regular. Contrarily, quasiperiodic or complex $N : M$ ($M > 1$) phase lockings may yield arrhythmias due to the different beat to beat intervals in a phase-locking period. Let us take 3:1 and 3:2 for example. In Fig. 4(a) at A=4, at $T_{sti} = 92$ ms the rhythm is 3:1 and at $T_{sti} = 196$ ms the rhythm is 3:2. The responding period in 3:1 is regular 276 ms, and the beat-to-beat interval in 3:2 is 329.1 ms and 258.9 ms, alternatively. On the other hand, the responses under intense stimulation are simple, which make the heart-rate regulation easy. Therefore, one may prefer high amplitude of stimulation in dealing with SAN arrhythmias. The bifurcations at low and high amplitude are very different, which have already been discussed by many researches [26,27]. In the next section, we will apply PRM to interpret the bifurcations.

## IV. THE PRM APPROACH TO STUDY PHASE-LOCKING BEHAVIORS

In the previous studies, phase response and the resulted PRMs of cardiac systems were measured and extensively used as powerful tools to analyze the bifurcation processes [14,26–29]. It is useful that the simple 1D PRM describes the bifurcations qualitatively and even can take the place of the high-dimensional differential equations. It was well elucidated that the types of bifurcation are closely related to the topological degree of the PRM [15,26–30]. Keener and Glass [27] gave a mathematical discussion in this aspect.

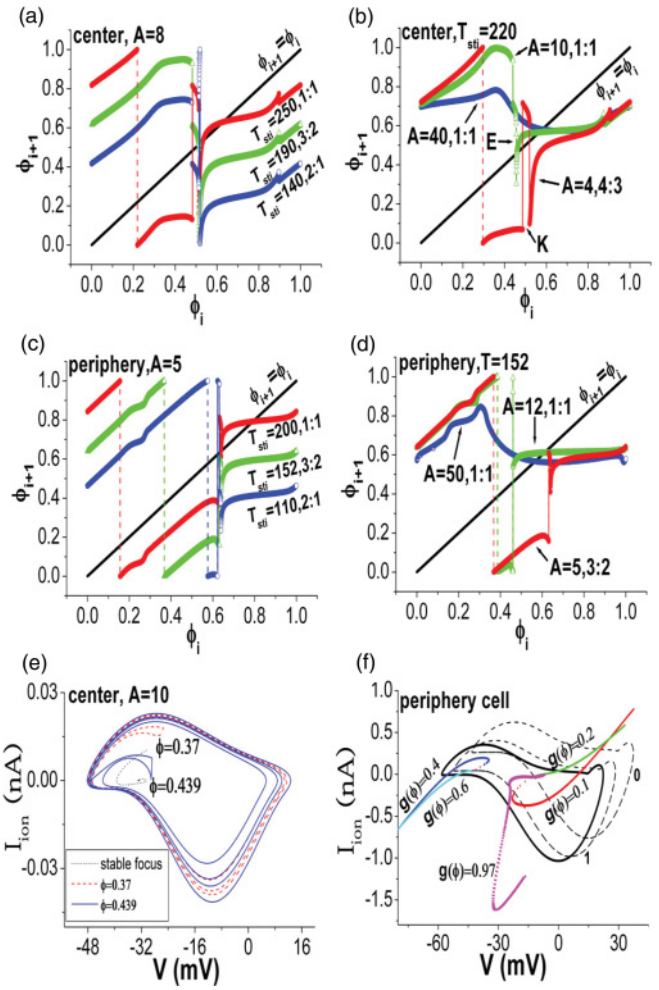


FIG. 5. (Color online) Phase-transition maps produced by varying stimulating period $T_{sti}$ and amplitude A. Parameters are given in each figure. Dashed vertical lines are used to connect the departed sections which are continuous, where the discontinuities are due to mod 1 operation. Solid vertical lines are used to connect discontinuous sections. (a), (b) The effects of $T_{sti}$ and A on the PRM of single-central cell, respectively. (c), (d) The effects of $T_{sti}$ and A on the PRM of single peripheral cell, respectively. PRM is shifted upward and downward by increasing and decreasing $T_{sti}$, while increase of the amplitude flips the right branches upward and tend to make the curve smooth. (e) The distortion of the trajectory in the vicinity of the unstable cycle, which yields sections of slope $< 0$ on the left branch of PRM. (f) Pseudo-isochrone distribution of the single peripheral cell. The solid cycle is the unperturbed limit cycle and the dashed ones are illustrations of the shifted cycles. The topology of PRM is determined by the relative position between the shifted cycle and the isochrones.

Tsalikakis *et al.* [34,40] measured the curve of $g(\phi)$ of Zhang's ionic SAN model. In this section, we aim at giving a description of the PRM of the present model. The parameters influence on PRM and the presentation of $N : M$ on the curve are illustrated.

The PRMs of central and peripheral cells are measured to qualitatively interpret the phase locking transitions of Fig. 4. It is illustrated in Fig. 5 that increasing and decreasing the period only shift the whole PRM upward and downward [Figs. 5(a) and 5(c)] while varying the amplitude can dramatically change

the shape of the curve [Figs. 5(b) and 5(d)]. Figures 5(a) and 5(c) show that in the 1:1 zone, the PRM and the straight line $\phi_{i+1} = \phi_i$ intersect at a fixed point, which is a stable solution because the absolute value of the slope of PRM at this point is less than 1. As the period is reduced, the PRM shifts downward and the fixed point is lost at a certain $T_{sti}$ value, then the iterated solution on PRM falls into a certain orbit and complex $N : M$ ($M > 1$) states occur. On the other hand, Figs. 5(b) and 5(d) show the bifurcations induced by varying amplitude: Increase of amplitude tends to tie the departed branches together and reduce the slope of the branches. The PRM thus tends to intersect the straight line $\phi_{i+1} = \phi_i$ at a sufficiently large A value and 1:1 occurs and maintains. Further increase of the amplitude will tie the PRM into a smooth curve [blue (dark gray) lines in Figs. 5(b) and 5(d)]. The flips of the right branches of Figs. 5(b) and 5(d) show the mechanism underlying the transitions from complex $N : M$ ($M > 1$) phase lockings to simple $N : 1$ lockings by increasing A.

The effect of increasing amplitude on PRM has been well studied by some authors [15,17,18,21,26–30]. By calculating the average slope of the curve, they defined the change as transition from topological degree 1 map to degree 0 map, and declared that different bifurcations occur in the above two cases. The present PRMs of SAN are similar to that measured by Refs. [18,28,30] in experiments of spontaneously beating embryonic chicken heart cell aggregates and that in model SAN cells [22,34]. At high amplitude, a continuous map (degree 0) is shown [blue (dark gray) line of Figs. 5(b) and 5(d)]. At intermediate and low amplitude, discontinuous maps are derived [green (light gray) and red (gray) lines of Figs. 5(b) and 5(d)]. However, the topological degree of the discontinuous map cannot be ascertained because the first transient phase is used in the present work. Two kinds of factors may contribute to the discontinuities. (i) The discontinuity occurs in the first transient phase (the measurement we take in the present work) and vanishes at the asymptotic phase (the $n$ th phase as $n \to \infty$). This kind of discontinuity is regarded as Kawato-type discontinuity [47]. The discontinuous site of the red (gray) line labeled "K" in Fig. 5(b) is an example of such discontinuity. (ii) The discontinuity is due to limited calculation and experiment precision. In some cases, the curve is likely continuous, but much more precise calculation and special techniques are needed to reveal the underlying continuity, as has been found by Krogh-Madsen *et al.* [48] in a different SAN model. This kind of discontinuity is regarded as effective discontinuity, which is labeled "E" on the green (light gray) line in Fig. 5(b), serving as a possible example. Detailed measurements of PRMs can be seen in Refs. [21,47,48]. In the discontinuous map of central cell, sections of slope $< 0$ apparently occur on the left branch of PRM [e.g., the green (light gray) line in Fig. 5(b)]. The reason may be that appropriate amplitude brings the trajectory to the vicinity of the unstable limit cycle, where the orbit may rotate [as shown in Fig. 5(e)], so that the time interval between the stimulus and the action potential following is lengthened, and the slope is changed.

As indicated by some previous works [17,21], the profound reason that amplitude can change the topology of PRM is related to the isochrones of the limit cycle in phase space. Phase points on an identical isochron possess identical value of $g(\phi)$. Figure 5(f) is an illustration of the theory. The flat portion of $g(\phi) = 0.97$ isochrone corresponds to the flat section of PRM at large $\phi$. It should be noted that the isochrone here is a bit different to Winfree's theory. Firstly, the first transient phase is used here instead of the asymptotic phase used by Winfree to measure isochrones. Secondly, the present isochrones are plotted in $I_{\text{ion}} - V$ plane, which were analyzed in the full phase space in Winfree's theory. Therefore, we call the isochrone in the present paper "pseudo-isochrone" for distinction. The pseudo-isochrones are constructed by the following way: At every state point on the unperturbed limit cycle, single stimulus with amplitude ranged from $-50$ to 50 (minus amplitude means hyperpolarized stimulating current) is applied directly to the membrane. Phase transition is measured for each amplitude value. After scanning the limit cycle, all state points giving a specific value of $g(\phi)$ after stimulations construct the $g(\phi)$ pseudo-isochrone. Note that when the stimulus is applied to the single equation about $V$ only, the isochrones in high-dimensional space (15D in the present model) are 1D curves (which are a subset of the 14D isochronal hypersurfaces in phase space), and all the 1D isochrones together with the limit cycle locate on a 2D hypersurface in phase space. Thus most of the topological characteristics on the 2D hypersurface can be kept in projection to the $I_{\text{ion}} - V$ phase plane. Therefore, we can discuss these 1D isochrones in the reduced two-variable phase plane.

A stimulus with a certain amplitude pulls the phase point to a certain pseudo-isochrone. If we apply stimulus at every point on the limit cycle with a certain fixed amplitude (this operation is equivalently to scan $\phi$ in the entire cycle with a fixed amplitude), all the phase points after stimulation make up a cycle called shifted cycle. If the amplitude is small, it pulls the cycle with a little deviation from the limit cycle and the shifted cycle can intersect with all the pseudo-isochrones [dashed cycle labeled 1 in Fig. 5(f)], so that monotonic PRM can be measured (corresponding to degree 1 map). But high amplitude may pull the cycle to a much larger distance so that the shifted cycle may not intersect with certain pseudo-isochrones [dashed cycle labeled 0 in Fig. 5(f)], and then the PRM is nonmonotonic (corresponding to nonmonotonic degree 1 or degree 0 map). The dashed curves in Fig. 5(f) are just illustrations of how the isochrone concept works, which are not produced by actual stimulations of certain given amplitudes. Details of the theory can be seen in Refs. [17,21,47].

We further discuss the presentation of $N : M$ phase locking on PRM. The 3:2 phase locking is taken as an example, which is shown in Fig. 6(a). In this case, any initial $\phi$ will fall into the orbit indicated by the arrowed lines. There are three horizontal arrowed lines and two downward vertical arrowed lines. There is a simple and useful rule to identify most of the $N : M$ phase lockings on PRM: $K + N : M$ ($K = 0,1,2\ldots$) phase lockings can be identified for any $K$ value by counting the $N$ horizontal and $M$ downward vertical lines, and if $nT_0 < T_{sti} < (n+1)T_0$ ($n = 0,1,2\ldots$) then $K = n$. If there is a stable intersected point of the line and PRM, 1:1 is determined and $K$ must be 0. However, the $2N : 2$ rhythm (e.g., 2:2, 4:2, and so on) zones which are narrow (as indicated by Guevara and Shrier [29]) cannot be identified by such a method. Calculating the rotation number is a much more precise method to identify $2N : 2$ states [Eq. (10)] [28]. Figure 6(b) shows the PRM of high amplitude

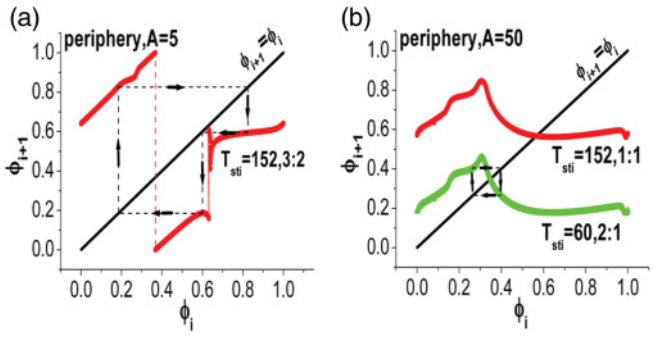


FIG. 6. (Color online) Graphic study of phase locking behaviors. (a) Orbit of 3:2 state on PRM. There are three horizontal arrowed lines and two downward vertical lines, so that it should be $K + 3 : 2$ ($K = 0,1\ldots$). (b) PRM at high amplitude. In this case, at most one downward arrowed line can occur in the graphic solution so that only ATs of $K + N : 1$ ($K = 0,1\ldots$) exist.

and explains the reason why only $N : 1$ class of ATs can be observed. In such a case, at most one downward line can occur in the orbit and $M$ must be 1. This is the mechanism for the direct $N : 1$ transitions at high amplitude. Specifically, the orbit shown in Fig. 6(b) is 2:1 rather than 2:2, which is calculated by the rotation number [Eqs. (8) and (10)].

It is meaningful that the phase-locking properties can be identified directly from the shape of the PRM ($N : M$ class refers to the $K + N : M$ phase lockings for any $K$ value): (i) If the branches of the curve have average slope sufficiently $> 0$ (the left branch may have a section of slope $> 0$ or slope $< 0$), complex $N : M$ may exist. (ii) If the right branches have average slope $\approx 0$, zones of $N : M$ ($M > 1$) class become very narrow (each $N : M$ zone occupies smaller than 1 ms of $T_{sti}$ in the "$T_{sti}$-A" parameter plane), and zones of $N : 1$ class occupy prevalently in parameter plane. (iii) If the slope of the right branches is apparently $< 0$, only simple $N : 1$ ($2N : 2$) class exist. (iv) Furthermore, if the curve is tied to be a smooth single peak curve, only simple 1:1 (2:2) and 2:1 classes exist. Tangent bifurcation occurs mainly in type (i) PRM [red (gray) line in Fig. 5(a)] and period doubling bifurcation occur popularly in type (iv) PRM [blue (dark gray) line in Fig. 5(a)]. Both tangent and period doubling bifurcations may occur in type (ii) and (iii) PRM.

## V. THE MEMORY EFFECT ON PRM

The original model consists of a set of differential equations (DEs) which construct a high-dimensional phase space (15D) while PRM is a simple 1D map. It might be rather surprising as well as interesting and useful if this much simplified map can still catch the main essence of the original SAN DEs. Besides the qualitative validity discussed in Sec. IV, the quantitative validity of PRM in describing the bifurcations should be discussed.

In order to evaluate the quantitative validity of the PRM description on phase-locking transitions, we compare the bifurcation diagrams derived from the PRM with those obtained directly from numerical simulations of the original DEs. The comparisons are done by single-central cell model with rotation number [Eqs. (8) and (10)] (the situations are similar

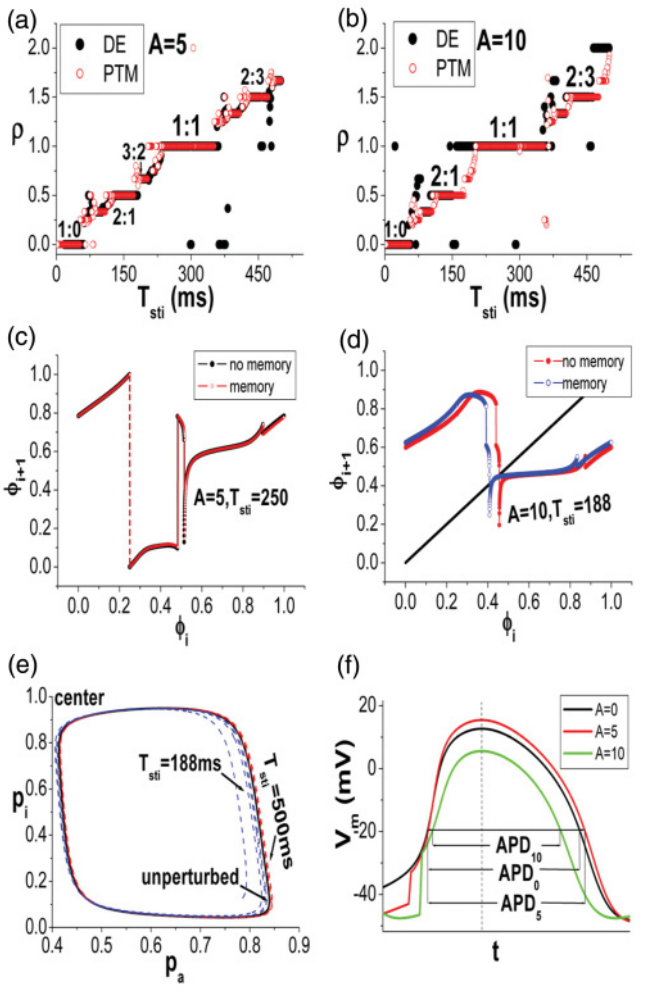


FIG. 7. (Color online) Quantitative validity of PRM. The investigations are done by single-central cell. Parameters are shown in figures. (a), (b) Comparison of the DE and PRM. Rotation number is used. At A = 5 the staircases of DE and PRM fit well with each other. At A = 10, obvious deviation between DE and PRM can be seen. (c), (d) Different degrees of memory effect at A = 5 and A = 10. (e) Representation of memory effect by two gating variables with longer time constants. A = 10. The state takes more time to return to the unperturbed cycle after faster stimulating. (f) APDs of periodic stimulation at different amplitudes. $T_{sti} = 250$ ms. The memory effect may be partly due to the APD rate dependence.

in peripheral cell). During the simulations, the initial value set of the DEs is given in the Appendix, and the initial value of $\phi$ is 0.5. The data are recorded after 200 000 simulation steps of DEs and 50 000 iterating steps of PRM. Figure 7 shows that at low amplitude, the bifurcation diagrams of both approaches fit well with each other [Fig. 7(a)]; But at higher amplitude, obvious difference between the two approaches appears [see Fig. 7(b)]. Many factors attribute to this phenomenon. We consider that the memory effect of DEs may play a role in determining the bifurcation structure, while this memory effect is completely neglected in PRM approach. However, it remains to be determined that the memory effect is the major factor accounting for the discrepancy seen in Figs. 7(a) and 7(b).

There are kinds of memory effect in biological systems. Especially, memory effect in spontaneously beating cell

systems were investigated in Ref. [49]. In the present work, we focus on the memory of action potential duration (APD). Generally the PRM is measured from initial condition of free running state (i.e., no stimulus is applied and the system oscillates at its intrinsic rhythm). But the shape and the location of PRM should depend on the stimulating history, which is termed as the memory effect. APD depends on the stimulating period, which is an intrinsic property of the cardiac cell [12]. The change of APD may influence PRM. We measure both the PRMs from the initial condition of free running state and from the initial condition after 100 stimulations. It is found that at low amplitude the discrepancy is slight [Fig. 7(c)] while at higher amplitude it becomes greater [Fig. 7(d)]. Figure 7(b) indicates that at $T_{sti} = 188$ ms, the phase locking should be 1:1, but the free running PRM [solid (gray) circles in Fig. 7(d)] has no intersection point on the line so that complex entrainment ($N : M$, $M > 1$) is anticipated. However, the PRM with memory effect [empty (dark gray) circles in Fig. 7(d)], which is measured after times of stimulation with period $T_{sti}$, intersects with the line at a stable fixed point, which implies 1:1 entrainment. The result of the memory PRM coincides better with the observation of the original DEs. In Fig. 7(e) the two gate variables determining the dynamics of the rectified potassium current $I_{Kr}$ (activation gate $p_a$ and inactivation gate $p_i$), which is the major current during repolarizing and diastolic depolarizing phase of the action potential, are chosen to construct a phase plane to show memory effect after rapid stimulating. The stimulation is stopped after hundreds of times. Then the state will recover to the unperturbed cycle (solid line). The variables have to take a longer time to return after rapid stimulating ($T_{sti} = 188$ ms, dashed blue line) than that after relatively slow stimulating ($T_{sti} = 500$ ms, dashed red line). That means the system remembers the pacing history to a larger extent at higher stimulating frequency. In Fig. 7(f) it can be seen that at high amplitude, APD is changed more dramatically by periodic stimulation, which contributes more to the memory effect. It should be emphasized that memory effect is due to stimulating rate rather than amplitude. Amplitude influences the intensity of memory effect when stimulating rate is changed.

Despite the quantitative deviation in describing the bifurcations for relatively higher amplitude, free running PRM is still a convenient and satisfactory method for analyzing the phase-locking behaviors. Firstly, it is time saving to measure the free running PRM. Secondly, although at high amplitude PRM cannot well predict phase lockings, the properties of bifurcation can be well judged from PRM by its shape, as is indicated by Figs. 6(a) and 6(b). At low amplitude, PRM can even be used to substitute DEs. At high amplitude, since that the memory effect partly comes from the APD rate dependence, a more precise derivation of PRM considering the APD restitution curve is waiting.

## VI. PHASE-LOCKING STRUCTURES OF THE HETEROGENOUS TISSUE

In the above sections we studied single-cell dynamics. The behaviors of tissue show more complicated as well as more interesting characteristics and they are significant for understanding the phase-locking behaviors of the realistic SAN. Cells in SAN are coupled by gap junctions, and synchronization of these cells is extremely important for the functions of SAN. The ability of synchronized pacemaking of the heart is partly determined by the coupling conductance [24,31,50–52]. Previous experimental studies measured that about 0.2–0.5 nS of the conductance is sufficient to synchronize the oscillations between two isolated cells [52]. We measure the threshold for synchronization of the present numerical model and find that about 3.4 nS is needed to synchronize the whole tissue (0.07 nS is needed to entrain a pair of center and periphery cells, larger coupling current is needed to entrain larger aggregate of cells). Figure 8(a) shows the maximum and minimum period in the cable as the coupling strength $G_{\rm cpl}$ is changed. When $G_{\rm cpl} > 3.4$ nS maximum and minimum period are nearly identical and the cells in tissue oscillates at a common period. Figure 8(b) is the synchronous spatiotemporal pattern. There is a wave-like propagation through the tissue, where the phase of the peripheral cell is advanced. As indicated by some experiments, if a segment of atrial muscle is linked to the SAN tissue, the phase leading site may be shifted by the coupling strength from the atrium [53].

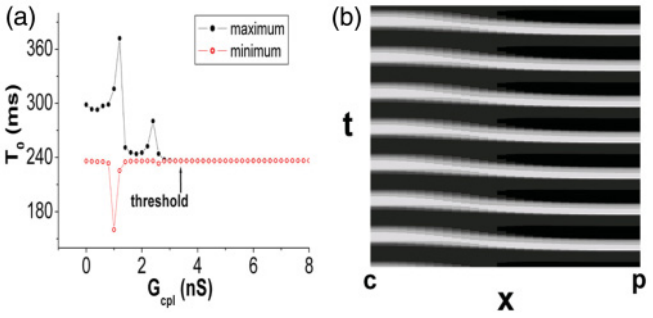


FIG. 8. (Color online) Synchronization of the tissue. (a) The maximum and minimum period in the cable depending on the coupling strength $G_{\rm cpl}$. The threshold for period synchronization of the whole tissue is about 3.4 nS. (b) $G_{\rm cpl} = 20$ nS. The spatiotemporal pattern of synchronous oscillation. From left to right is center to periphery.

We stimulate either the center or periphery end of the same tissue, and record the data of the cell 2 mm distant from the stimulated end in each case. Figure 9 show the phase locking structures under relatively low- and high-coupling strength [20 nS for (a), (b) and 50 nS for (c) (d)]. Although 3.4 nS is sufficient for frequency synchronization, stronger coupling is needed for emergence of certain locking zones in distant sites, because at low coupling the propagation ability is weak. It is interesting that the ATs of the center-stimulated and periphery-stimulated cases are qualitatively different. In center-stimulated tissue, as shown by Figs. 9(a) and 9(c), the ATs obeying Farey's tree grow well with the amplitude to a very high level. However, in periphery-stimulated tissue [Figs. 9(b) and 9(d)], the complex $N : M$ ($M > 1$) ATs are blocked (or they only occur in a very narrow range smaller than 1 ms) and $N : 1$ ($2N : 2$) ATs remain. Moreover, the $2N : 2$ zones of periphery-stimulated tissue are gradually excluded as the coupling is increased.

The PRMs of the stimulated central cell and stimulated peripheral cell at different amplitudes are plotted in Figs. 10(a)

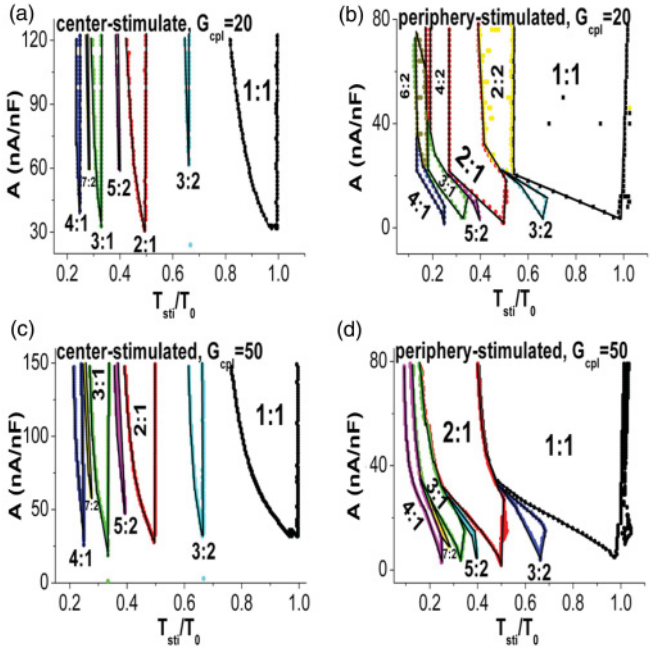


FIG. 9. (Color online) Arnold tongues of the heterogeneous 1D tissue. Data are recorded from the grid point 2 mm distant from the stimulated site. The abscissa is the ratio of the stimulating period to the common period of the tissue. (a), (b) The ATs of the center-stimulated and the periphery-stimulated tissue at $G_{\rm cpl} = 20$ nS. (c), (d) The ATs at $G_{\rm cpl} = 50$ nS. The phase-locking properties of either stimulated case remain as $G_{\rm cpl}$ varies.

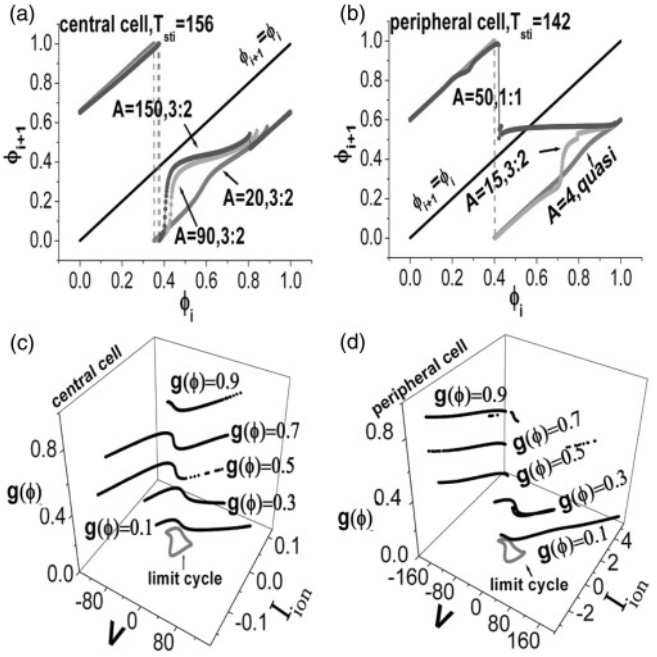


FIG. 10. (Color online) PRMs and pseudo-isochrones of the stimulated cell in center- and periphery-stimulated tissue. $G_{\rm cpl} = 20$ nS. Other parameters are shown in the figure. (a), (b) PRMs of stimulated ends of center- and periphery-stimulated cases, respectively. Variation of A changes the central PRM weakly while it changes that of peripheral PRM dramatically. (c), (d) Pseudo-isochrone distributions of stimulated central and peripheral cells. We plot the pseudo-isochrones in a three dimensional space to distinguish them from each other. At $V > 0$ half of the space, nearly all pseudo-isochrones remain for central cell but many do not exist for peripheral cell.

and 10(b). The phase response of the 1D tissue of Zhang's model have been measured by Tsalikakis *et al.* [40] by applying stimulus to every cell instantaneously in the tissue. In the present study, we only stimulate the cell at either end of the tissue. For strong coupling, PRMs of the cell at stimulated end can reveal the bifurcations of the tissue. Increasing amplitude can easily flip the right part of the peripheral PRM while its influence on the central PRM is much weaker. As discussed in Sec. IV, at high amplitude, the central PRM corresponds to shape (i) so that $N : M$ ($M > 1$) states exist, and the peripheral PRM shows shape (ii) so that mainly $N : 1$ ($2N : 2$) can be seen. Figures 10(c) and 10(d) reveal the pseudo-isochrones of the central end cell and peripheral end cell in tissue. In order to distinguish them from each other we add the $Z$ axis of $g(\phi)$ so that each pseudo-isochrone locates at a layer uniquely. The distributions are very different in the two instances. In the central case, nearly all pseudo-isochrones exist in the $V > 0$ half of the plane, but in the peripheral case many pseudo-isochrones do not exist in the $V > 0$ half of the plane. The external stimuli applied to the tissue are injected inward current, which increases the $V$, so that the shifted cycle in center stimulated case can intersect with all the pseudo-isochrones in high-dimensional space but not in the periphery stimulated case. This is the reason why a very large amplitude maintains the topological degree of the central PRM but a little larger amplitude change the shape of peripheral PRM dramatically. Another factor that may influence the phase locking structure is the change of capacitance along the cable. Since the phase-locking data are collected from the site distant to the stimulated end, the ability for the fast stimulated end synchronizing the distant site should influence phase locking. Even if larger capacitance cells (periphery) impose a larger load to neighboring cells, they provide a larger magnitude of current to the neighbors when excited. So that it is relatively easier for the larger capacitance cells stimulating the smaller capacitance cells than the reverse case. Therefore we can observe larger phase-locking zones in the peripheral-stimulated case.

Our results indicate that the phase locking behaviors of SAN responding to the electrical perturbations closely relate to the perturbing sites. The difference between center- and periphery-stimulated phase lockings may provide ideas to control heart rhythm by properly choosing the stimulating sites in tissue.

The influence of $G_{\rm cpl}$ on phase locking is also investigated in the present work. Figure 11 shows the ATs of center- and periphery-stimulated tissues in the "$T_{sti}$-$G_{\rm cpl}$ " plane. The stimulating amplitude is fixed and $G_{\rm cpl}$ is varied in the range that synchronized pacing of the free running tissue is realized. The data are recorded from the cell 2 mm distant from the stimulated end. Interestingly, the growing trends of the tongues in center-stimulated and periphery-stimulated tissues are opposite. As $G_{\rm cpl}$ is increased, the phase-locking ranges of the center-stimulated tissue are enlarged, while those of the periphery-stimulated one are decreased. However, at high amplitude of periphery-stimulated tissue, it seems that the zones of 1:1, 2:1, etc., become large as $G_{\rm cpl}$ is increased [Figs. 9(b) and 9(d)]. The reason is that the $2N : 2$ zones

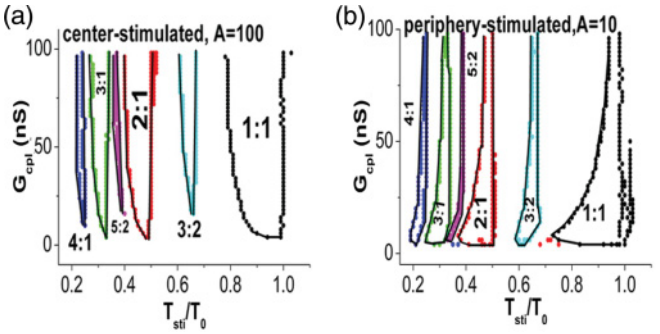


FIG. 11. (Color online) Arnol'd tongues growing with the coupling strength $G_{cpl}$. Data are recorded from the cell 2 mm distant from the stimulated site. The abscissa is the ratio of the stimulating period to the common period of the tissue of each $G_{cpl}$ value. Parameters are shown in the figures. (a) The ATs of the center-stimulated tissue. The zones are enlarged as $G_{cpl}$ is increased. (b) The inverse situation of periphery-stimulated tissue.

shrinks as $G_{cpl}$ is increased, and $N:1$ zones take the place of them. If we take each $N:1$ and the corresponding $2N:2$ zone as one whole zone, the whole zone still shrinks as $G_{cpl}$ is increased.

We try to interpret the phenomenon intuitively via simple analysis. Figures 12(a) and 12(b) are PRMs measured from the central and peripheral end, which reveals the effect of $G_{cpl}$ on the PRMs. The amplitude for each case is fixed. Change of $G_{cpl}$ does not change the topological degree of PRM. From this point of view, it is reasonable that low

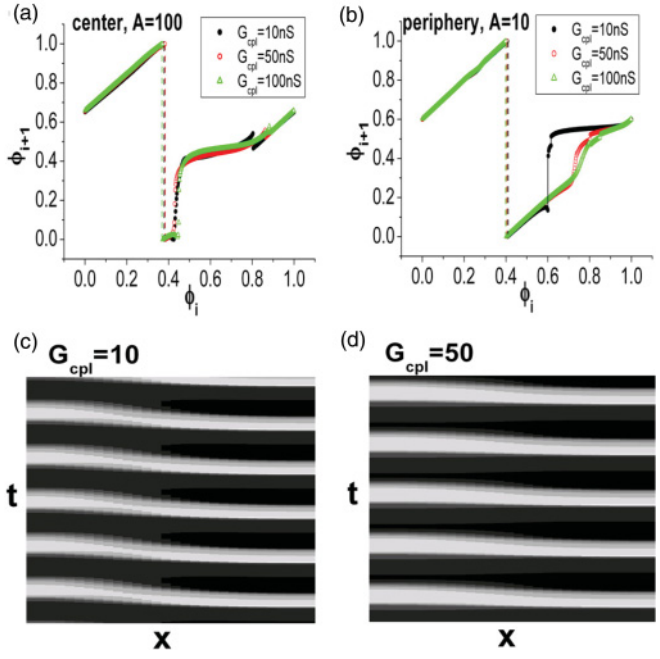


FIG. 12. (Color online) PRMs and patterns responding to variation of $G_{cpl}$. Parameters are shown in the figures. (a) The effect of $G_{cpl}$ variation on central PRM. The PRM changes little. (b) Much greater effect of $G_{cpl}$ variation on peripheral PRM. (c) Pattern at low $G_{cpl}$, which shows obvious phase difference along the medium. (d) Pattern at high $G_{cpl}$. Strong coupling reduces the phase difference along the tissue.

and high couplings retain the properties of phase locking in center- and periphery-stimulated cases. However, $G_{cpl}$ effect on central PRM is much weaker than that on peripheral PRM. We conjecture that the situation in center-stimulated case may be due to phase difference along the medium, while that in periphery-stimulated case is related to the excitation threshold of the stimulated cell itself. Figures 12(c) and 12(d) are the spatiotemporal patterns under low and high coupling. The phase propagation speed of high coupling is faster than that of low coupling. For center stimulus, at low coupling, it is difficult for the phase resetting information propagating to the distant end because it goes along in the converse direction of the phase propagation (in the coupled tissue, phase shift of one cell may trigger certain phase shift of its neighbor, we call this chain activity phase resetting information propagation, which is just an expression), while at high coupling, the phase difference becomes smaller, and the propagation of the phase resetting information becomes relatively easy. For periphery stimulus, increase of the coupling may increase the excitation threshold of the cell, so that the flat section of the right branch on the PRM at low coupling becomes inclined when coupling is increased. The effect of increasing $G_{cpl}$ is similar to the effect of decreasing amplitude A in the stimulated peripheral end.

The $G_{cpl}$ effect on the width of phase locking zones is significant for modulating the heart rhythm. The change of $G_{cpl}$ may be realized by drug therapy or some experimental techniques. It is expected that our results may provide ideas for practical treatment. Moreover, experimental and theoretical studies found that there is a spatial gradient of $G_{cpl}$ in the SAN tissue [54,55]. The effects of $G_{cpl}$ heterogeneity on phase locking need further investigations. The difference of phase locking properties between center- and periphery-stimulated cases reveals that the heterogeneity of the SAN tissue plays an important role in determining the phase-locking structures.

## VII. CONCLUSION

In the present work, we investigated the heterogeneous gradient SAN model. The phase-locking structures of the single central and peripheral cells of this model were elucidated. In both single central and peripheral cells, it is found that as the amplitude is increased, the complex phase locking zones ($N:M$ with $M>1$) are blocked and the simple locking behaviors ($N:1$ and $2N:2$) are retained. As a much simplified 1D map, PRM qualitatively explains and predicts the phase locking behaviors. Furthermore, we evaluated the quantitative validity of PRM in describing phase lockings of the original SAN DEs. At low amplitude, PRM can take the place of DEs with qualitative and quantitative precision; but at relatively high amplitude, PRM shows quantitative deviation which may be due to memory effect caused by APD rate dependence. It is interesting that the phase-locking behaviors are very different in the tissue when we stimulate the tissue at central end and periphery end. All the ATs obeying Farey's tree grow well when the central cell is stimulated. On the other hand, the $N:M$ ($M>1$) ATs shrink and only $N:1$ ($2N:2$) ATs remain finally when we do the same at the peripheral end. The phenomena are mainly due to the different distributions of pseudo-isochrone. The coupling strength in tissue is another

important parameter modulating phase lockings. We found that the growing trends of the ATs in center-stimulated and periphery-stimulated tissues are opposite, which were never noticed and may be significant for medical care. The results indicate that amplitude, stimulating site and coupling strength are the three most important parameters influencing phase locking behaviors in heterogenous SAN tissue.

The advantage of our results isthat the bifurcations and phase-locking features are obtained in an ionic SAN model where parameters represent practical SAN measurable quantities. Therefore, the phenomena revealed in the present work are expected to be experimentally realizable, which may provide suggestive instructions for practical treatment.

## ACKNOWLEDGMENTS

This work was supported by the National Natural Science Foundation of China under Grants No. 10675020 and 10975015 and by the National Basic Research Program of China (973 Program) under Grant No. 2007CB814800 and by the Science Foundation of Baoji University of Arts and Sciences under Grant No. ZK1048.

## APPENDIX: THE EQUATIONS IN THE MODEL AND INITIAL VALUES FOR SIMULATION

In solving the gating variable equation $\frac{dy}{dt} = \frac{y_\infty - y}{\tau_y}$, $y_\infty$ and $\tau_y$ are constants determined by $V$. The equations used in our work are

$$I_{\mathrm{Na}} = g_{\mathrm{Na}} m^3 h [\mathrm{Na}^+]_o \frac{F^2}{RT} \frac{e^{(V-E_{\mathrm{Na}})F/RT} - 1}{e^{VF/RT} - 1} V,$$

$$h = (1 - F_{\mathrm{Na}})h_1 + F_{\mathrm{Na}} h_2,$$

$$F_{\mathrm{Na}} = \frac{9.52 \times 10^{-2} e^{-6.3\times 10^{-2}(V+34.4)}}{1.0 + 1.66 e^{-0.225(V+63.7)}} + 8.69 \times 10^{-2},$$

$$m_\infty = \left( \frac{1}{1 + e^{-\frac{V}{5.46}}} \right)^{1/3},$$

$$\tau_m = \frac{0.6247}{0.832 e^{-0.335(V+56.7)} + 0.627 e^{0.082(V+65.01)}} + 4 \times 10^{-2},$$

$$h_{1\infty} = \frac{1}{1 + e^{\frac{V+66.1}{6.4}}},$$

$$\tau_{h_1} = \frac{3.717 \times 10^{-3} e^{-0.2815(V+17.11)}}{1 + 3.732 \times 10^{-3} e^{-0.3426(V+37.76)}} + 5.977 \times 10^{-1},$$

$$h_{2\infty} = h_{1\infty},$$

$$\tau_{h_2} = \frac{3.186 \times 10^{-5} e^{-0.6219(V+18.8)}}{1 + 7.189 \times 10^{-5} e^{-0.6683(V+34.07)}} + 3.556.$$

$$I_{\mathrm{Ca,L}} = g_{\mathrm{Ca,L}} \left[ f_L d_L + \frac{0.006}{1.0 + e^{-(V+14.1)/6.0}} \right] (V - E_{\mathrm{Ca,L}}),$$

$$d_{L\infty} = \frac{1}{1 + e^{-\frac{V+23.1}{6}}}, \quad \tau_{d_L} = \frac{1}{\alpha_{d_L} + \beta_{d_L}},$$

$$\alpha_{d_L} = \frac{-0.02839(V+35)}{e^{-\frac{V+35}{2.5}} - 1} - \frac{0.0849V}{e^{-0.208V} - 1},$$

$$\beta_{d_L} = \frac{0.01143(V-5)}{e^{0.4(V-5)} - 1},$$

$$f_{L\infty} = \frac{1}{1 + e^{-\frac{V+45}{5}}},$$

$$\tau_{f_L} = 257.1 e^{-\left(\frac{V+32.5}{13.9}\right)^2} + 44.3,$$

$$I_{\mathrm{Ca,T}} = g_{\mathrm{Ca,T}} d_T f_T (V - E_{\mathrm{Ca,T}}),$$

$$d_{T\infty} = \frac{1}{1 + e^{-\frac{V+37}{6.8}}}, \quad \tau_{d_T} = \frac{1}{\alpha_{d_T} + \beta_{d_T}},$$

$$\alpha_{d_T} = 1.068 e^{\frac{V+26.3}{30}}, \quad \beta_{d_T} = 1.068 e^{-\frac{V+26.3}{30}},$$

$$f_{T\infty} = \frac{1}{1 + e^{\frac{V+71}{9}}}, \quad \tau_{f_T} = \frac{1}{\alpha_{f_T} + \beta_{f_T}},$$

$$\alpha_{f_T} = 0.0153 e^{-\frac{V+61.7}{83.3}}, \quad \beta_{f_T} = 0.015 e^{\frac{V+61.7}{15.38}},$$

$$I_{\mathrm{to}} = g_{\mathrm{to}} q r (V - E_{\mathrm{K}}), \quad I_{\mathrm{sus}} = g_{\mathrm{sus}} r (V - E_{\mathrm{K}}),$$

$$q_\infty = \frac{1}{1 + e^{\frac{V+59.37}{13.1}}},$$

$$\tau_q = 10.1 + \frac{65.17}{0.57 e^{-0.08(V+49)} + 0.024 e^{0.1(V+50.93)}},$$

$$r_\infty = \frac{1}{1 + e^{-\frac{V-10.93}{19.7}}},$$

$$\tau_r = 2.98 + \frac{15.9}{1.037 e^{0.09(V+30.61)} + 0.369 e^{-0.12(V+23.84)}},$$

$$I_{\mathrm{K,r}} = g_{\mathrm{K,r}} p_a p_i (V - E_{\mathrm{K}}),$$

$$p_a = (1 - F_{\mathrm{K,r}}) p_{a,f} + F_{\mathrm{Kr}} p_{a,s}, \quad F_{\mathrm{K,r}} = 0.4,$$

$$p_{a,f\infty} = \frac{1}{1 + e^{-\frac{V+23.2}{10.6}}},$$

$$\tau_{p_{a,f}} = \frac{1}{37.2 \times 10^{-3} e^{\frac{V-9}{15.9}} + 0.96 \times 10^{-3} e^{-\frac{V-9}{22.5}}},$$

$$p_{a,s\infty} = \frac{1}{1 + e^{-\frac{V+23.2}{10.6}}},$$

$$\tau_{p_{a,s}} = \frac{1}{4.2 \times 10^{-3} e^{\frac{V-9}{17}} + 0.15 \times 10^{-3} e^{-\frac{V-9}{21.6}}},$$

$$p_{i\infty} = \frac{1}{1 + e^{\frac{V+18.6}{10.1}}}, \quad \tau_{p_i} = 0.002,$$

$$I_{\mathrm{K,s}} = g_{\mathrm{K,s}} x_s^2 (V - E_{\mathrm{K,s}}),$$

$$x_{s\infty} = \frac{\alpha_{x_s}}{\alpha_{x_s} + \beta_{x_s}}, \quad \tau_{x_s} = \frac{1}{\alpha_{x_s} + \beta_{x_s}},$$

$$\alpha_{x_s} = \frac{14 \times 10^{-3}}{1 + e^{-\frac{V-40}{9}}}, \quad \beta_{x_s} = 1 \times 10^{-3} e^{-\frac{V}{45}},$$

$$I_{\mathrm{f}} = g_{\mathrm{f,Na}} y (V - E_{\mathrm{Na}}) + g_{\mathrm{f,K}} y (V - E_{\mathrm{K}}),$$

$$y_\infty = \frac{1}{1 + e^{\frac{V+64}{13.5}}}, \quad \tau_y = \frac{1}{\alpha_y + \beta_y},$$

TABLE I. Parameters for central cell and peripheral cell. "c" means value for central cell and "p" means value for peripheral cell. "c,p" means the value is identical in both types of cell.

| | c | p | | c,p |
|---|---|---|---|---|
| $C_m$(pF) | 20 | 65 | $d_{\mathrm{NaCa}}$ | 0.0001 |
| $g_{\mathrm{Na}}(\mu\mathrm{S})$ | 0 | $1.2\times10^{-6}$ | $\gamma_{\mathrm{NaCa}}$ | 0.5 |
| $g_{\mathrm{Ca,L}}(\mu\mathrm{S})$ | $0.58\times10^{-2}$ | $6.59\times10^{-2}$ | $[\mathrm{Ca}^{2+}]_{\mathrm{o}}$(mM) | 2 |
| $g_{\mathrm{Ca,T}}(\mu\mathrm{S})$ | $0.43\times10^{-2}$ | $1.39\times10^{-2}$ | $[\mathrm{Ca}^{2+}]_{\mathrm{i}}$(mM) | 0.0001 |
| $g_{\mathrm{to}}(\mu\mathrm{S})$ | $4.91\times10^{-3}$ | $36.49\times10^{-3}$ | $[\mathrm{K}^{+}]_{\mathrm{o}}$(mM) | 5.4 |
| $g_{\mathrm{sus}}(\mu\mathrm{S})$ | $6.65\times10^{-5}$ | $1.14\times10^{-2}$ | $[\mathrm{K}^{+}]_{\mathrm{i}}$(mM) | 140 |
| $g_{\mathrm{K,r}}(\mu\mathrm{S})$ | $7.97\times10^{-4}$ | $1.6\times10^{-2}$ | $\mathrm{K}_{\mathrm{m,K}}$ | 0.621 |
| $g_{\mathrm{K,s}}(\mu\mathrm{S})$ | $5.18\times10^{-4}$ | $1.04\times10^{-2}$ | $\mathrm{K}_{\mathrm{m,Na}}$ | 5.64 |
| $g_{\mathrm{f,Na}}(\mu\mathrm{S})$ | $5.48\times10^{-4}$ | $0.69\times10^{-2}$ | $[\mathrm{Na}^{+}]_{\mathrm{i}}$(mM) | 8 |
| $g_{\mathrm{f,K}}(\mu\mathrm{S})$ | $5.48\times10^{-4}$ | $0.69\times10^{-2}$ | $[\mathrm{Na}^{+}]_{\mathrm{o}}$(mM) | 140 |
| $g_{\mathrm{b,Na}}(\mu\mathrm{S})$ | $5.8\times10^{-5}$ | $1.89\times10^{-4}$ | $F_{\mathrm{Kr}}$ | 0.4 |
| $g_{\mathrm{b,Ca}}(\mu\mathrm{S})$ | $1.32\times10^{-5}$ | $4.3\times10^{-5}$ | $F$ (C/mmol) | 96.5 |
| $g_{\mathrm{b,K}}(\mu\mathrm{S})$ | $2.52\times10^{-5}$ | $8.19\times10^{-5}$ | $R$ (J/mol· K) | 8.314 |
| $k_{\mathrm{NaCa}}$(nA) | $0.27\times10^{-5}$ | $0.88\times10^{-5}$ | $T$ (K) | 310 |
| $\bar{i_{\mathrm{p}}}$(nA) | $4.78\times10^{-2}$ | 0.16 | | |

$$\alpha_y = e^{-\frac{V+78.91}{26.62}}, \quad \beta_y = e^{\frac{V+75.13}{21.25}},$$

$$I_{\mathrm{b,Na}} = g_{\mathrm{b,Na}}(V - E_{\mathrm{Na}}), \quad I_{\mathrm{b,K}} = g_{\mathrm{b,K}}(V - E_{\mathrm{K}}),$$

$$I_{\mathrm{b,Ca}} = g_{\mathrm{b,Ca}}(V - E_{\mathrm{Ca}}),$$

$$I_{\mathrm{NaCa}} = \frac{k_{\mathrm{NaCa}}[\mathrm{Na}^{+}]_{\mathrm{i}}^3[\mathrm{Ca}^{2+}]_{\mathrm{o}}e^{0.03743V\gamma_{\mathrm{NaCa}}}}{1+d_{\mathrm{NaCa}}\left([\mathrm{Ca}^{2+}]_{\mathrm{i}}[\mathrm{Na}^{+}]_{\mathrm{o}}^3+[\mathrm{Ca}^{2+}]_{\mathrm{o}}[\mathrm{Na}^{+}]_{\mathrm{i}}^3\right)} - \frac{k_{\mathrm{NaCa}}[\mathrm{Na}^{+}]_{\mathrm{o}}^3[\mathrm{Ca}^{2+}]_{\mathrm{i}}e^{0.0374V(\gamma_{\mathrm{NaCa}}-1.0)}}{1+d_{\mathrm{NaCa}}\left([\mathrm{Ca}^{2+}]_{\mathrm{i}}[\mathrm{Na}^{+}]_{\mathrm{o}}^3+[\mathrm{Ca}^{2+}]_{\mathrm{o}}[\mathrm{Na}^{+}]_{\mathrm{i}}^3\right)},$$

$$I_{\mathrm{p}} = \bar{i_{\mathrm{p}}}\left(\frac{[\mathrm{Na}^{+}]_{\mathrm{i}}}{K_{\mathrm{m,Na}}+[\mathrm{Na}^{+}]_{\mathrm{i}}}\right)^3\left(\frac{[\mathrm{K}^{+}]_{\mathrm{o}}}{K_{\mathrm{m,K}}+[\mathrm{K}^{+}]_{\mathrm{o}}}\right)^2 \times \frac{1.6}{1.5+e^{-(V+60)/40}},$$

$$E_{\mathrm{Na}} = \frac{RT}{F}ln\frac{[\mathrm{Na}^{+}]_{\mathrm{o}}}{[\mathrm{Na}^{+}]_{\mathrm{i}}}, \quad E_{\mathrm{Ca}} = \frac{RT}{2F}ln\frac{[\mathrm{Ca}^{2+}]_{\mathrm{o}}}{[\mathrm{Ca}^{2+}]_{\mathrm{i}}},$$

$$E_{\mathrm{K}} = \frac{RT}{F}ln\frac{[\mathrm{K}^{+}]_{\mathrm{o}}}{[\mathrm{K}^{+}]_{\mathrm{i}}}, \quad E_{\mathrm{K,s}} = \frac{RT}{F}ln\frac{[\mathrm{K}^{+}]_{\mathrm{o}}+0.12[\mathrm{Na}^{+}]_{\mathrm{o}}}{[\mathrm{K}^{+}]_{\mathrm{i}}+0.12[\mathrm{Na}^{+}]_{\mathrm{i}}},$$

$$E_{\mathrm{Ca,T}} = 45\ \mathrm{mV}, \quad \mathrm{E}_{\mathrm{Ca,L}} = 46.4\ \mathrm{mV}.$$

The parameters in the model are set by the values in Table I. In addition, some authors (e.g., Garny *et al.* [56]) noted that there are some incorrectly published equations in the initial paper [33]. The correct equations of Zhang's model can be found at the COR (cellular open resource) website [57].

The initial values are:

Central cell: $V=-51.44$; $m=0.124$; $h_1=0.595$; $h_2=5.25\times10^{-2}$; $d_L=5.912\times10^{-2}$; $f_L=0.825$; $d_T=0.106$; $f_T=0.119$; $y=3.775\times10^{-2}$; $r=3.924\times10^{-2}$; $q=0.358$; $x_s=5.7\times10^{-2}$; $p_{a,f}=0.47$; $p_{a,s}=0.637$; $p_i=0.965$.

Peripheral cell: $V=-64.35$; $m=0.124$; $h_1=0.595$; $h_2=5.25\times10^{-2}$; $d_L=8.45\times10^{-2}$; $f_L=0.987$; $d_T=1.725\times10^{-2}$; $f_T=0.436$; $y=5.28\times10^{-2}$; $r=1.97\times10^{-2}$; $q=0.663$; $x_s=7.67\times10^{-2}$; $p_{a,f}=0.4$; $p_{a,s}=0.327$; $p_i=0.991$.

In simulations of the cable, initial values of all grid points are set uniformly by that identical to single-central cell.

The dynamics of a single cell is governed by a set of 15 ODEs. The local stability of a state point is determined by the eigenvalues of the Jacobian matrix. At the stable and unstable fixed points, we have values of $V$ and gating variables so that elements in the matrix can be calculated. At stable fixed point the eigenvalues are (the first value is the real part and the second is the imaginary part, and all real parts are negative):

$$\begin{pmatrix} -499.9646, & 0 \\ -7.3637, & 0 \\ -8.87, & 0 \\ -2.2003, & 0 \\ -0.7015, & 0 \\ -1.0732, & 0 \\ -0.1074, & -1.5167\times10^{-2} \\ -0.1074, & 1.5167\times10^{-2} \\ -2.237\times10^{-2}, & 0 \\ -1.8279\times10^{-3}, & -1.062\times10^{-2} \\ -1.8279\times10^{-3}, & 1.062\times10^{-2} \\ -4.3494\times10^{-3}, & 0 \\ -1.1259\times10^{-3}, & 0 \\ -2.0905\times10^{-3}, & 0 \\ -0.264, & 0 \end{pmatrix}.$$

Eigenvalues of the unstable fixed point are (two of them have positive real part):

$$\begin{pmatrix} -499.9838, & 0 \\ -5.416, & 0 \\ -2.3791, & 0 \\ -6.0138, & 0 \\ -0.7414, & 0 \\ -0.3563, & 0 \\ -0.1387, & 0 \\ -6.4994\times10^{-2}, & 0 \\ 1.2848\times10^{-2}, & -8.651\times10^{-4} \\ 1.2848\times10^{-2}, & 8.651\times10^{-4} \\ -1.5635\times10^{-2}, & 0 \\ -1.2571\times10^{-3}, & 0 \\ -4.9697\times10^{-3}, & 0 \\ -5.3391\times10^{-2}, & 0 \\ -2.4251\times10^{-3}, & 0 \end{pmatrix}.$$

[1] P. F. Cranefield, A. L. Wit, and B. F. Hoffman, Circulation **47**, 190 (1973).
[2] M. E. Mangoni and J. Nargeot, Physiol. Rev. **88**, 919 (2008).
[3] J. K. Choate, F. R. Edwards, G. D. S. Hirst, and J. E. O'Shea, J. Physiol. **471**, 707 (1993).
[4] D. C. Michaels, E. P. Matyas, and J. Jalife, Circ. Res. **55**, 89 (1984).
[5] D. C. Michaels, D. R. Chialvo, E. P. Matyas, and J. Jalife, Circ. Res. **65**, 1350 (1989).
[6] W. Mobitz, Z. Ges. Exp. Med. **41**, 180 (1924).
[7] B. van der Pol and J. van der Mark, Phil. Mag. Suppl. **6**, 763 (1928).
[8] H.-X. Wang, R. de Paola, and W. I. Norwood, Phys. Rev. Lett. **70**, 3671 (1993).
[9] D. Cai, Y.-C. Lai, and R. L. Winslow, Phys. Rev. Lett. **71**, 2501 (1993).
[10] C. D. Wagner and P. B. Persson, Cardiovasc. Res. **40**, 257 (1998).
[11] O. Kongas, R. von Hertzen, and J. Engelbrecht, Chaos Solitons Fractals **10**, 119 (1999).
[12] A. Karma and J. Robert F. Gilmour, Phys. Today **60(3)**, 51 (2007).
[13] L. Glass, A. L. Goldberger, M. Courtemanche, and A. Shrier, Proc. R. Soc. London A **413**, 9 (1987).
[14] J. M. Anumonwo, M. Delmar, A. Vinet, D. C. Michaels, and J. Jalife, Circ. Res. **68**, 1138 (1991).
[15] V. C. Kowtha, A. Kunysz, J. R. Clay, L. Glass, and A. Shrier, Prog. Biophys. Molec. Biol. **61**, 255 (1994).
[16] L. Glass, Chaos **1**, 13 (1991).
[17] A. T. Winfree, *The Geometry of Biological Time*, 2nd ed. (Springer-Verlag, New York, 2001).
[18] M. R. Guevara, L. Glass, and A. Shrier, Science Wash. DC **214**, 1350 (1981).
[19] D. G. Bristow and J. W. Clark, Am. J. Physiol. **12**, H207 (1982).
[20] M. R. Guevara and A. Shrier, Biophys. J. **52**, 165 (1987).
[21] M. R. Guevara and H. J. Jongsma, Am. J. Physiol. **27**, H734 (1990).
[22] A. C. F. Coster and B. G. Celler, Ann. Biomed. Eng. **31**, 271 (2003).
[23] J. Jalife, V. A. Slenter, J. J. Salata, and D. C. Michaels, Circ. Res. **52**, 642 (1983).
[24] D. C. Michaels, E. P. Matyas, and J. Jalife, Circ. Res. **58**, 706 (1986).
[25] H. Croisier, M. R. Guevara, and P. C. Dauby, Phys. Rev. E **79**, 016209 (2009).
[26] M. R. Guevara and L. Glass, J. Math. Biology **14**, 1 (1982).
[27] J. P. Keener, J. Math. Biology **21**, 175 (1984).
[28] L. Glass, M. R. Guevara, J. Belair, and A. Shrier, Phys. Rev. A **29**, 1348 (1984).
[29] M. R. Guevara and A. Shrier, Ann. N.Y. Acad. Sci. **591**, 11 (1990).
[30] W.-Z. Zeng, M. Courtemanche, L. Sehn, A. Shrier, and L. Glass, J. Theor. Biol. **145**, 225 (1990).
[31] J. Jalife, J. Physiol. **356**, 221 (1984).
[32] M. R. Boyett, H. Honjo, and I. Kodama, Cardiovasc. Res. **47**, 658 (2000).
[33] H. Zhang, A. V. Holden, I. Kodama, H. Honjo, M. Lei, T. Varghese, and M. R. Boyett, Am. J. Physiol. **279**, H397 (2000).
[34] D. G. Tsalikakis, H. G. Zhang, D. I. Fotiadis, G. P. Kremmydas, and L. K. Michalis, Comp. Biol. Med. **37**, 8 (2007).
[35] E. E. Verheijck, A. Wessels, A. C. G. van Ginneken, J. Bourier, M. W. M. Markman, J. L. M. Vermeulen, J. M. T. de Bakker, W. H. Lamers, T. Opthof, and L. N. Bouman, Circulation **97**, 1623 (1998).
[36] H. Zhang, A. V. Holden, and M. R. Boyett, Circulation **103**, 584 (2001).
[37] Y. Kurata, I. Hisatome, S. Imanishi, and T. Shibamoto, Am. J. Physiol. **283**, 2074 (2002).
[38] J. W. Moore and F. Ramon, J. Theor. Biol. **45**, 249 (1974).
[39] S. Rush and H. Larsen, IEEE Trans. Biomed. Eng. **25**, 389 (1978).
[40] D. G. Tsalikakis, D. I. Fotiadis, L. K. Michalis, and G. P. Kremmydas, IEEE Trans. Biomed. Eng. **54**, 1710 (2007).
[41] V. I. Arnol'd, Am. Math. Soc. Transl. (2) **46**, 213 (1965).
[42] L. Glass and R. Perez, Phys. Rev. Lett. **48**, 1772 (1982).
[43] L. Glass and J. Sun, Phys. Rev. E **50**, 5077 (1994).
[44] J. R. Clay, M. R. Guevara, and A. Shrier, Biophys. J. **45**, 699 (1984).
[45] E. N. Best, Biophys. J. **27**, 87 (1979).
[46] L. Glass and A. T. Winfree, Am. J. Physiol. **246**, R251 (1984).
[47] M. Kawato, J. Math. Biol. **12**, 13 (1981).
[48] T. Krogh-Madsen, L. Glass, E. J. Doedel, and M. R. Guevara, J. Theor. Biol. **230**, 499 (2004).
[49] A. Kunysz, L. Glass, and A. Shrier, Am. J. Physiol. **269**, H1153 (1995).
[50] D. C. Michaels, E. P. Matyas, and J. Jalife, Circ. Res. **61**, 704 (1987).
[51] J. Jalife, D. C. Michaels, and M. Delmar, Prog. Clin. Biol. Res. **275**, 67 (1988).
[52] E. E. Verheijck and R. Wilders, J. Gen. Physiol. **111**, 95 (1998).
[53] I. Kodama and M. R. Boyett, Pfluegers Arch. **404**, 214 (1985).
[54] W. K. Bleeker, A. J. Mackaay, M. Masson-Pevet, L. N. Bouman, and A. E. Becker, Circ. Res. **46**, 11 (1980).
[55] R. W. Joyner and F. J. L. van Capelle, Biophys. J. **50**, 1157 (1986).
[56] A. Garny, P. Kohl, P. J. Hunter, M. R. Boyett, and D. Noble, J. Cardiovasc. Electrophysiol. **14**, S121 (2003).
[57] [http://cor.physiol.ox.ac.uk/].